

Arctic Mixed-Phase Cloud Properties from AERI Lidar Observations: Algorithm and Results from SHEBA

D. D. TURNER

Pacific Northwest National Laboratory, Richland, Washington

(Manuscript received 5 September 2003, in final form 7 September 2004)

ABSTRACT

A new approach to retrieve microphysical properties from mixed-phase Arctic clouds is presented. This mixed-phase cloud property retrieval algorithm (MIXCRA) retrieves cloud optical depth, ice fraction, and the effective radius of the water and ice particles from ground-based, high-resolution infrared radiance and lidar cloud boundary observations. The theoretical basis for this technique is that the absorption coefficient of ice is greater than that of liquid water from 10 to 13 μm , whereas liquid water is more absorbing than ice from 16 to 25 μm . MIXCRA retrievals are only valid for optically thin ($\tau_{\text{visible}} < 6$) single-layer clouds when the precipitable water vapor is less than 1 cm. MIXCRA was applied to the Atmospheric Emitted Radiance Interferometer (AERI) data that were collected during the Surface Heat Budget of the Arctic Ocean (SHEBA) experiment from November 1997 to May 1998, where 63% of all of the cloudy scenes above the SHEBA site met this specification. The retrieval determined that approximately 48% of these clouds were mixed phase and that a significant number of clouds (during all 7 months) contained liquid water, even for cloud temperatures as low as 240 K. The retrieved distributions of effective radii for water and ice particles in single-phase clouds are shown to be different than the effective radii in mixed-phase clouds.

1. Introduction

The atmospheric circulation and, hence, the climate are driven by the influx of solar energy and outflow of longwave energy, which heats and cools the planet, respectively. Clouds play a critical role in the redistribution of the solar and infrared energy fluxes, and, thus, the basic physics of how these clouds interact with the radiation field must be well understood if it is to be correctly represented in climate models.

Clouds both scatter and absorb solar and infrared radiation. The amount of scattering and absorption depends on the thermodynamic phase, size, shape, and density of the cloud particles. The phase of the cloud must be known first, because the refractive properties of ice and water can be markedly different, depending on the wavelength. Historically, many studies have either focused on low-level clouds, which are warm and assumed to be entirely composed of liquid water droplets, or high clouds that are very cold and composed of only ice particles. However, many clouds are composed of both water and ice particles, that is, they are mixed-phase clouds. Treating this class of clouds as a single-

phase cloud can lead to significant biases in model simulations (Sun and Shine 1995; Gregory and Morris 1996).

From a climate change point of view, accurate determination of cloud properties, and, in particular, the identification of cloud phase, is most critical in the Arctic. Curry et al. (1996) have identified cloud phase as one of the primary unknowns in the Arctic. Significant errors in the radiative fluxes at the surface and top of the atmosphere can result if the cloud phase is incorrectly specified. This can lead to errors in the modeled longwave radiative flux at the surface, which can have important affects in global climate models by altering the freezing and melting rate of the ice in the Arctic in the spring and autumn transition seasons (Jiang et al. 2000). Furthermore, several modeling studies have shown that the Arctic is particularly sensitive to changes in atmospheric composition, which is connected with the cloud properties through a variety of feedback mechanisms, and it is theorized that any climate change should be noticed first in this region (Houghton et al. 1992). This makes long time series of Arctic cloud properties critical to evaluating any climate change scenario.

To determine cloud phase with passive remote sensing instruments, the observations must encompass wavelengths where the absorption coefficient for ice changes significantly with respect to the absorption co-

Corresponding author address: Dave Turner, Climate Physics Group, MS K9-24, Pacific Northwest National Laboratory, P.O. Box 999, Richland, WA 99352.
E-mail: dave.turner@pnl.gov

efficient of water. For example, Fig. 1 demonstrates that the ice absorption is greater than that of liquid water from 10 to 13 μm and is less than the absorption coefficient of liquid water from 16 to 25 μm . The Atmospheric Emitted Radiance Interferometer (AERI) instrument (Knuteson et al. 2004) makes observations in both of these spectral regions. Turner et al. (2003) have demonstrated that cloud phase can be determined from these ground-based, high-spectral-resolution infrared radiance observations. Daniel et al. (2002) also retrieved cloud phase by using a spectral region where the absorption coefficient of ice and water changes significantly (850–1050 nm), although their results are restricted to daytime periods.

The outline of this paper is as follows. A short overview of the instruments used in this analysis is presented in section 2. The mixed-phase cloud property retrieval algorithm (MIXCRA) is described in section 3, and results from a series of simulations are discussed in section 4. Two case studies, which compare the MIXCRA retrievals with other techniques in single-phase clouds, are presented and discussed in section 5. MIXCRA was applied to 7 months of data collected during the Surface Heat Budget of the Arctic Ocean (SHEBA; Uttal et al. 2002) experiment; these results are discussed in section 6. The paper ends with a summary and conclusions in section 7.

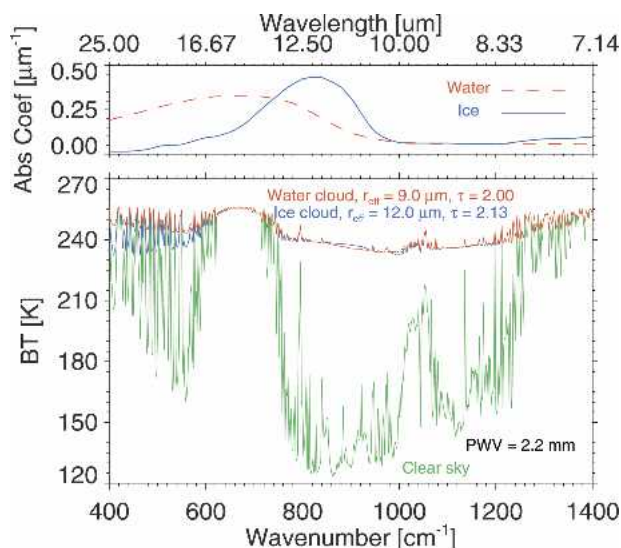


FIG. 1. (top) The absorption coefficients of liquid water and ice, and (bottom) downwelling infrared spectra computed with LBLDIS for a clear-sky scene (green) and for the same atmosphere with an ice cloud (blue) and a liquid cloud (red) at 600 m. The microphysical properties of the ice cloud were chosen such that the brightness temperature spectrum of 8–13 μm was nearly identical with the spectrum associated with the liquid cloud; however, note that the 10–20-K differences in the 16–25- μm window allow the cloud phase to be determined. The change in the transparency of the 16–25- μm window results in a 4.1 W m^{-2} difference in cloud forcing between the two cases, where the cloud forcings for the ice and water cloud cases are 61.3 and 65.4 W m^{-2} , respectively.

2. Instruments

a. AERI

The AERI is a fully automated ground-based passive infrared interferometer. The AERIs deployed in the Arctic measure downwelling atmospheric radiance spectra from 400 to 3000 cm^{-1} (2.5–3.3 μm), with a spectral resolution of approximately 1 cm^{-1} . AERIs have been deployed at many locations around the world, including during SHEBA and at the U.S. Department of Energy's Atmospheric Radiation Measurement (ARM) North Slope of Alaska (NSA) site in Barrow, Alaska (Stamnes et al. 1999; Knuteson et al. 2004).

A typical AERI measurement cycle consists of a 3-min sky-view period, followed by 2-min view periods at each of the two high-emissivity (>0.995) calibration blackbodies. One blackbody is fixed at 60°C while the other is at ambient temperature, and these temperatures are monitored with high-precision thermistors (Minnett et al. 2001). This measurement strategy allows the AERI to be self-calibrated for each observation cycle, resulting in absolute calibration accuracy that is better than 1% of the ambient radiance. More information on the AERI instrument, including details on the radiometric and spectral calibration, can be found in Knuteson et al. (2004).

b. Depolarization and Backscatter Unattended Lidar

During SHEBA, a polarization-sensitive lidar was deployed near the AERI. The National Oceanic and Atmospheric Administration (NOAA) Environmental Technology Laboratory (ETL) Depolarization and Backscatter Unattended Lidar (DABUL) is a compact, autonomous lidar system, designed to produce research-quality measurements of backscatter and depolarization ratio measurements from clouds and aerosols (Alvarez et al. 1998). The nominal vertical and temporal resolutions of the DABUL are 30 m and 5 s, but the temporal resolution was degraded for this analysis to improve the signal-to-noise ratio. The DABUL data used in this study had a temporal resolution 10 min, which is close to the AERI's temporal resolution. The lidar-observed cloud boundaries (Intrieri et al. 2002), together with temperature profiles observed by radiosondes, are a critical input to the cloud property retrieval algorithm.

3. Algorithm

Turner et al. (2003) demonstrated that cloud phase could be determined using ground-based AERI observations in both the 8–13- and 17–25- μm windows by using a series of threshold tests. MIXCRA extends those results by physically retrieving cloud optical depth due to water and ice (τ_w and τ_i , respectively) and the effective sizes of the water ($r_{e,w}$) and ice ($r_{e,i}$) par-

ticles. Ice fraction is then computed as $f_i = \tau_i / (\tau_i + \tau_w)$. The optical depth data shown in this paper are all referenced to the visible (i.e., where the extinction efficiency is 2).

a. Forward model

The forward model utilized in this work is a combination of the Line-by-Line Radiative Transfer Model (LBLRTM; Clough and Iacono 1995), which computes the gaseous optical depth profiles as a function of wavelength, and the Discrete Ordinate Radiative Transfer (DISORT) code (Stamnes et al. 1988), which accounts for the scattering and absorption of the cloud and completes the radiative transfer. This combined model will hereinafter be referred to as LBLDIS. The LBLRTM has been extensively validated against the AERI in clear-sky scenes (Turner et al. 2004). This work used version 6.1 of the LBLRTM, the water vapor continuum model CDK 2.4, and the high-resolution transmission molecular absorption (HITRAN) 2000 line database. During SHEBA, radiosondes were launched at least twice daily and were used to specify the temperature and moisture structure of the atmosphere for the LBLDIS calculations. The DISORT calculations used 16 streams, and the angular distribution of the scattering was prescribed by the Henyey–Greenstein function.

The single scattering properties for liquid water droplets, which are required for the forward model, are calculated from the Lorentz–Mie theory (using Wiscombe 1980), with the refractive indices taken from Downing and Williams (1975). Observations by a Cloud Particle Imager (CPI) in springtime Arctic clouds during the First International Satellite Cloud Climatology Project (ISCCP) Regional Experiment (FIRE) Arctic Cloud Experiment (ACE) indicate that many of the small cloud ice particles are “spheroids” (Lawson et al. 2001). Therefore, ice crystals are modeled both as spheres, using refractive indices from Warren (1984), and as a combination of more realistic shapes. The latter model uses droxtals (Yang et al. 2003), which are very similar to spheres, except with flat faces, for ice crystals with effective radii of $\leq 16 \mu\text{m}$, and hexagonal columns (Yang et al. 2001) for the larger ice crystals. At the transition point of $16 \mu\text{m}$, the aspect ratio of both the droxtals and hexagonal columns is unity. This ice model will be referred to as the droxtal–hexcolumn model. The single scattering properties for all ice habits assume that the density of the ice is 917 kg m^{-3} . A gamma size distribution is used for both water and ice particles, as discussed in Turner et al. (2003). It should be noted that the effective radius utilized in this work is proportional to the ratio of the volume to the projected area of the size distribution of the crystals. The scattering properties for the different habits have been integrated over the size distribution for different effective radii and stored into a “scattering database” for the physical retrieval algorithm. The scat-

tering properties of mixed-phase clouds were computed by linearly combining the scattering properties as a function of optical depth of liquid droplets and ice crystals following Sun and Shine (1995).

b. Cloud emissivity

Water vapor is an extremely strong absorber/emitter of radiation across the IR spectrum, and, therefore, any algorithm that attempts to ascertain cloud properties using observations in this spectral region must account for the water vapor. By utilizing cloud emissivity as the “observed” variable in any cloud property algorithm, the impact of changing water vapor burdens can be minimized. Following Smith et al. (1993), the cloud emissivity ε_c derived from downwelling infrared radiance observations R^\downarrow can be written as

$$\varepsilon_c = \frac{R^\downarrow - R_{\text{clr}}^\downarrow - r_c(\mathfrak{T}_s^c)^2[(B(T_s)\varepsilon_s)]}{\mathfrak{T}_s^c B(T_c)}, \quad (1)$$

where $R_{\text{clr}}^\downarrow$ is the clear-sky downwelling radiation, r_c is the cloud reflectivity, ε_s is the surface emissivity, \mathfrak{T}_s^c is the transmission from the surface to the cloud, B is the Planck function, and T_s and T_c are the temperatures of the surface and cloud, respectively. All variables, except the surface and cloud temperatures, are assumed to have a wavelength dependence. Note that ε_c is a function of τ , f_i , $r_{e,w}$, and $r_{e,i}$ (the variables we wish to retrieve).

The advantage of high-spectral-resolution observations, such as from the AERI, is that a cloud property retrieval algorithm can utilize “microwindows” between gaseous absorption lines, thereby minimizing the effects of the atmospheric gases. The microwindows utilized in this work are given in Table 1. However, the cloud-to-surface transmission term \mathfrak{T}_s^c complicates the derivation of the cloud emissivity. In the Arctic, \mathfrak{T}_s^c is very close to unity for microwindows between 8 and $13 \mu\text{m}$ because of the very low amounts of water vapor present and, thus, can be assumed to be one. However,

TABLE 1. Center wavelength and wavenumber ranges for each microwindow used in the physical retrieval.

Center wavelength (μm)	Wavenumber range (cm^{-1})	Center wavelength (μm)	Wavenumber range (cm^{-1})
20.90	477.5–479.5	11.19	891.9–895.8
20.13	495.5–498.0	11.09	898.2–905.4
18.84	529.9–531.5	10.70	929.6–939.7
17.85	558.5–562.0	10.39	959.9–964.3
12.94	770.9–774.8	10.09	985.0–998.0
12.69	785.9–790.7	9.25	1076.6–1084.8
12.33	809.0–812.9	9.13	1092.1–1098.8
12.20	815.3–824.4	8.97	1113.3–1116.6
12.03	828.3–834.6	8.86	1124.4–1132.6
11.83	842.8–848.1	8.73	1142.2–1148.0
11.60	860.1–864.0	8.63	1155.2–1163.4
11.43	872.2–877.5		

this term cannot be set to unity in the 17–25- μm region because of the strength of the water vapor absorption in this spectral region and needs to be estimated from the LBLRTM clear-sky calculations.

c. Cloud reflectivity

Cloud reflectivity in the infrared is fairly small and generally is assumed to be negligible (e.g., DeSlover et al. 1999; Smith et al. 1999). However, because Arctic clouds are close to the surface (Intrieri et al. 2002), which emits a significant amount of radiation relative to the atmospheric emission, the cloud reflectivity should not be ignored. To compute the cloud reflectivity, we hold the cloud properties constant and compute downwelling radiance twice, where the forward calculations differ only by a perturbation to the surface radiance term $B(T_s)\epsilon_s$. Because the atmospheric and cloud properties are unchanged for the two calculations, we can set the two calculations in Eq. (1) equal to each other and rearrange to solve for r_c as

$$r_c = \frac{R_1^\downarrow - R_2^\downarrow}{\mathfrak{I}_s^c[B(T_{s,1})\epsilon_{s,1} - B(T_{s,2})\epsilon_{s,2}]}, \quad (2)$$

where R_1^\downarrow and R_2^\downarrow are the downwelling radiance calculations for the corresponding surface conditions. This allows the spectral cloud reflectivity to be calculated. It should be noted that perturbing the surface temperature by 1, 10, or 20 K yields almost exactly the same reflectivity spectrum, as do reasonable (i.e., <10%) changes in the surface emissivity.

The cloud reflectivity spectrum is a function of the single scattering properties of the clouds. Examples of cloud reflectivity spectra are given in Fig. 2. Ice clouds have significantly more reflectance from 400 to 550 cm^{-1} than liquid water clouds, which is consistent with the fact that ice is less absorbing in this spectral region. Also note that the reflectivity spectrum is a function of optical depth, but that $\partial r_c / \partial \tau$ is small when $\tau > 5$. The reflectivity spectra associated with optically thick clouds are consistent with the results from Herman (1980), who indicated that the infrared broadband cloud reflectivity approaches a maximum value of 2% for optically thick clouds.

d. MIXCRA

MIXCRA uses an optimal estimation approach (e.g., Rodgers 2000), which propagates uncertainties in the observed variable (the cloud emissivity spectrum \mathbf{Y}) and forward model into the retrieved state vector $\mathbf{X} = (\tau_w, \tau_i, r_{e,w}, r_{e,i})$. Because the radiative transfer includes scattering, which is highly nonlinear, the MIXCRA uses a physical iterative approach. The formulation of the retrieval is given by (Rodgers 2000)

$$\begin{aligned} \mathbf{X}^{n+1} = & \mathbf{X}_a + (\mathbf{S}_a^{-1} + \mathbf{K}^T \mathbf{S}_e^{-1} \mathbf{K})^{-1} \{ \mathbf{K}^T \mathbf{S}_e^{-1} [\mathbf{Y} - F(\mathbf{X}^n)] \\ & + \mathbf{K}(\mathbf{X}^n - \mathbf{X}_a) \}, \end{aligned} \quad (3)$$

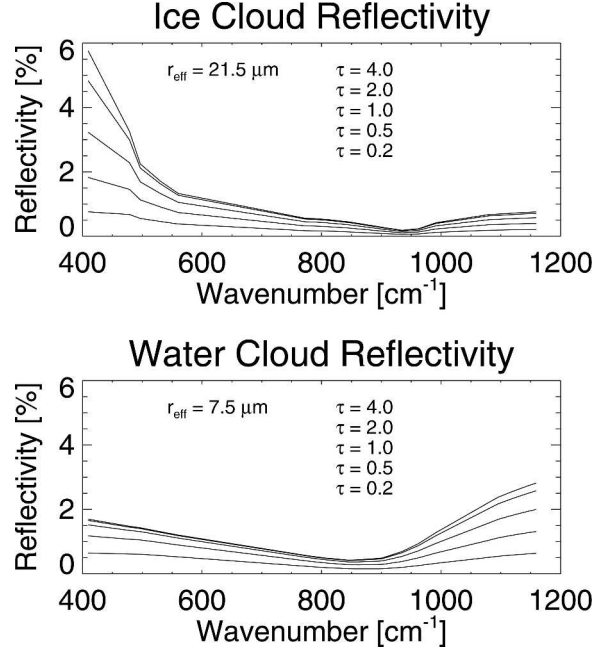


FIG. 2. Infrared cloud reflectivity spectra for various optical depths of (top) ice ($r_e = 21.5 \mu\text{m}$) and (bottom) water ($r_e = 7.5 \mu\text{m}$) clouds. Smaller optical depths have reflectivities closer to zero.

where n is the iteration number. The superscripts T and -1 indicate matrix transpose and inverse, respectively. The a priori state vector \mathbf{X}_a and its covariance \mathbf{S}_a are discussed shortly. The forward model F is LBLDIS. The Jacobian \mathbf{K} is the sensitivity of the emissivity spectrum to the state vector, and is defined as $(\mathbf{K})_{ij} = \partial \epsilon_i / \partial X_j$. Because of the nonlinearity of the problem, \mathbf{K} is estimated for each iteration using finite differences. The optimal estimation formulation provides the 1- σ error estimates \mathbf{e}_x for the state vector \mathbf{X} as (Rodgers 2000)

$$\mathbf{e}_x \mathbf{e}_x^T = (\mathbf{S}_a^{-1} + \mathbf{K}^T \mathbf{S}_e^{-1} \mathbf{K})^{-1}. \quad (4)$$

The cloud emissivity spectrum is a function of the observed radiance \mathbf{I} , clear-sky radiance (which is primarily a function of the precipitable water vapor P because the algorithm utilizes microwindows), and the effective cloud temperature T ; therefore, the uncertainties in all three of these terms must be propagated into the observation covariance matrix \mathbf{S}_e . If we denote the clear-sky model calculation by the operator F , the Planck function by the operator B , and the emissivity calculation by the operator G , we can write

$$\boldsymbol{\epsilon} = G[\mathbf{I}, B(T), F(P)]. \quad (5)$$

Using the standard technique to propagate errors (Bevington and Robinson 1992), the covariance matrix \mathbf{S}_e is computed as

$$\begin{aligned} \mathbf{S}_e = & \mathbf{K}_{GI} \mathbf{S}_I \mathbf{K}_{GI}^T + \mathbf{K}_{GB} \mathbf{K}_{BT} \mathbf{S}_T \mathbf{K}_{BT}^T \mathbf{K}_{GB}^T \\ & + \mathbf{K}_{GF} \mathbf{K}_{FP} \mathbf{S}_P \mathbf{K}_{FP}^T \mathbf{K}_{GF}^T. \end{aligned} \quad (6)$$

The matrix \mathbf{K}_{ab} , which defines any arbitrary Jacobian in Eq. (6), is given by

$$(\mathbf{K}_{ab})_{ij} = \partial \mathbf{a}_i / \partial \mathbf{b}_j \quad (7)$$

for any vector or operator \mathbf{a} and \mathbf{b} .

The AERI instrument noise is assumed to be spectrally uncorrelated; that is, the matrix \mathbf{S}_I is assumed to be diagonal. However, the uncertainties in cloud temperature and water vapor result in emissivity uncertainties that are correlated with wavelength, resulting in nonzero entries for the off-diagonal elements of \mathbf{S}_e . The uncertainty in the precipitable water vapor was assumed to be 5%. The cloud temperature is a DABUL backscatter-weighted average from the radiosonde profile, and the uncertainty in this quantity is a function of the separation of the cloud layers (Turner 2003).

Equation (3) utilizes an a priori state vector \mathbf{X}_a in the retrieval. Often, \mathbf{X}_a is developed from climatology, but because there are little data on the variation of cloud optical depth, ice fraction, or particle size in the Arctic, \mathbf{X}_a and its covariance matrix \mathbf{S}_a are crudely estimated. The default particle sizes for water and ice are 7 and 21 μm , respectively, as suggested by the CPI observations (Turner et al. 2003); but the associated uncertainties in these values are set to be 10 and 20 μm , respectively, so as to not be a serious constraint. The total cloud optical depth $\tau = \tau_w + \tau_i$ is approximated as a simple polynomial function of the cloud emissivity at 900 cm^{-1} , and the initial guess of the ice fraction is 50%. These values provide estimates for the optical depths for the water and ice components in \mathbf{X}_a . The associated uncertainties in optical depth are set to 5, which is large enough to not be a serious constraint on these retrievals. The off-diagonal elements in \mathbf{S}_a are assumed to be zero.

The advantage of using \mathbf{X}_a in this formulation is that additional knowledge can easily be added to the MIXCRA retrievals. For example, if the cloud temperature is above 0°C, then it is highly unlikely that the cloud will contain any significant amount of ice, and, therefore, \mathbf{X}_a can be used to “turn off” the ice component of the retrieval. By setting the optical depth due to ice in \mathbf{X}_a to zero, and its associated variance in \mathbf{S}_a to a value very near zero (such as 10^{-10}), the MIXCRA retrieval is effectively a single-phase retrieval and is only able to retrieve the optical depth and particle size of the water component. Likewise, if the cloud is colder than -40°C , then MIXCRA automatically converts to an ice-only retrieval.

e. Water path calculations

Most global climate and cloud resolving models predict liquid and ice water paths; therefore, measurements of these parameters are important for validating and improving these models. If the effective size of the particle is large with respect to the wavelength, then a simple relationship exists between water path (W), visible optical depth (τ_{vis}), and effective radius (r_e) for spherical particles (e.g., Stephens 1994):

$$W = \frac{2 r_e \rho \tau_{\text{vis}}}{3}, \quad (8)$$

where ρ is the bulk density of the water substance (liquid or ice). The liquid water path (LWP) is computed for each MIXCRA retrieval by transforming the retrieved optical depth at 11 μm into a visible optical depth by $\tau_{\text{vis}} = \tau_{\text{IR}} Q_{e,\text{vis}} / Q_{e,\text{IR}}$. Note that the visible extinction efficiency $Q_{e,\text{vis}}$ is assumed to be the asymptotic limit of 2 [consistent with the formulation of Eq. (8)], and that the infrared extinction efficiency $Q_{e,\text{IR}}$ is integrated over the droplet size distribution.

Ice particles are typically not spheres; therefore, MIXCRA allows the ice particles to be any shape by using different precomputed single scattering property databases. As described in section 3a, these databases consist of the single scattering properties for a given particle shape integrated over a given size distribution (such as a gamma distribution with a width factor of 0.1) for a range of effective radii. For each effective radius, the total volume of the ice crystals $V_0(r_{e,i})$ is computed and stored in the database, as well as the total number density of the ice particles $N_0(r_{e,i})$. After MIXCRA retrieves τ_i and $r_{e,i}$ for the overhead cloud, the integrated number density is computed as $N(r_{e,i}, \tau_i, z) = \tau_i / [k(r_e)z]$, where z is the cloud geometric thickness determined from the lidar cloud boundaries and $k(r_e)$ is the extinction cross section that is determined from the scattering database. The ice water path (IWP) can then be derived from the following relation:

$$\text{IWP} = \frac{N(r_{e,i}, \tau_i, z)}{N_0(r_{e,i})} V_0(r_{e,i}) \rho_i z, \quad (9)$$

where ρ_i is bulk density of the ice, which is what was used in the computation of the ice single scattering properties (Yang et al. 2001, 2003). Note that different habits have different values of V_0 for the same value of r_e ; this term essentially captures the dependence of effective density as a function of habit. Simulations have shown that the IWP computed for a cloud consisting of ice spheres, using the “volume based” derivation given by Eq. (9) and the “spherical” algorithm given by Eq. (8), are identical. However, when computing the uncertainty in the IWP by propagating the uncertainties in the retrieved variables τ_i and $r_{e,i}$, the uncertainty in the volume-based algorithm is slightly larger (approximately 5%) than the uncertainty computed using the spherical algorithm due primarily to the added uncertainty in determining V_0 . However, the volume-based derivation given in Eq. (9) allows IWP to be computed for any particle habit.

The MIXCRA-retrieved ice cloud optical depth and ice fraction (τ_i and f_i , respectively) are not very sensitive to the assumed habit of the ice particles. Typically, the differences in the retrieved τ_i and f_i were approximately 1% and 5%, respectively, (such as for the cirrus cloud shown in Fig. 6) when the crystals were modeled

as spheres versus the droxtal-hexcolumn model. However, the retrieved value of the ice particle size ($r_{e,i}$) is sensitive to the assumed habit of the ice crystals. This leads to differences in the IWP that are occasionally as large as a factor of 2 when the ice particles are assumed to be composed of droxtal-hexcolumn crystals relative to when the ice particles are assumed to be spherical. Many retrieval techniques show similar sensitivities to the assumed ice habit (Comstock et al. 2004). A more detailed investigation of how to determine the appropriate ice habit to utilize in this retrieval algorithm is beyond the scope of this paper.

4. Simulations

A series of simulations were used to characterize the influence of biases on the retrieval algorithm and to ascertain if the retrieved $1\text{-}\sigma$ uncertainty values [Eq. (4)] were representative of the true uncertainties in the retrieved values. The LBLDIS model was used to simulate over 100 different Arctic clouds. The primary atmosphere used in these simulations was specified by a SHEBA radiosonde on 25 April 1998 that had a precipitable water vapor (PWV) of 2.45 mm, but other Arctic atmospheres were also utilized with very similar results. Only single-layer clouds were simulated. The clouds were primarily placed at 600 m, which corresponds roughly to the peak of the cloud height distribution, as suggested by Intrieri et al. (2002).

MIXCRA showed very little sensitivity with height; that is, if the same cloud was placed at different altitudes, the retrieved microphysical properties were nearly identical as long as the specified cloud temperature was correct for each case. The uncertainty in cloud emissivity due to the uncertainty in cloud temperature is relatively flat across the spectrum, and, correspondingly, small biases in the cloud temperature that were used in computing the emissivity translate into relatively flat biases in the computed emissivity. Therefore, small positive (negative) biases in the cloud temperature result in negative (positive) biases in the total optical depth. Small biases in the cloud temperature do not affect the spectral signature of the cloud emissivity, and, thus, the retrieved ice fraction and particle sizes are essentially unaffected by small biases in cloud temperature.

Water vapor absorption is a strong function of wavelength, with the absorption being much stronger in the 400–600 than in the 800–1200 cm^{-1} region. This is illustrated in Fig. 3, where a 5% uncertainty in PWV dominates at the longer wavelengths. Because the 400–600 cm^{-1} region is critical for the correct determination of cloud phase, the retrieved ice fraction is sensitive to biases in PWV. The impact on the retrieved ice fraction depends on the amount of PWV and the optical thickness and phase of the cloud.

Simulations were also conducted to evaluate the im-

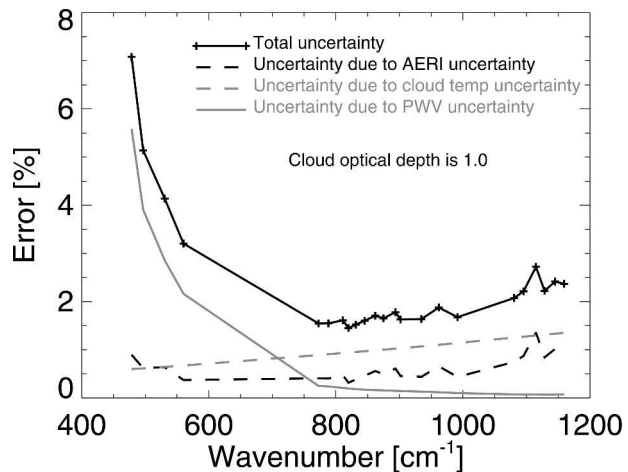


FIG. 3. Typical uncertainty in the emissivity spectrum, separated into its three components, for a cloud with optical depth of 1 for an atmosphere with PWV = 2.45 mm. The ordinate is the relative error in cloud emissivity (i.e., $100 \sigma_e / \epsilon$). The uncertainty in water vapor is the dominant term in the emissivity uncertainty in the Arctic window from 400 to 600 cm^{-1} .

pact on the retrieved cloud properties for the small approximately 1 $\text{mW} (\text{m}^2 \text{ster cm}^{-1})^{-1}$ spectrally flat bias that may exist in the AERI observations (Turner et al. 2003; Turner 2003; Marty et al. 2003). These simulations suggested that a bias of this size only affects the retrievals if the cloud optical depth is small ($\tau \sim 0.2$), wherein the bias is approximately 25%–50% of the cloud signal. As τ becomes larger, a small spectrally flat bias becomes negligible. However, Sassen and Comstock (2001) have shown that nearly half of the cirrus at a midlatitude site have optical depths less than 0.3, and so research is continuing to determine the source of this bias.

To evaluate the skill of the MIXCRA for different cloud conditions, each of the simulated clouds was replicated and instrument noise was added. The instrument noise was assumed to be Gaussian with the standard deviation provided by the AERI's noise spectrum. An ensemble of typically 60 individual spectra was created for each simulated cloud. MIXCRA was then used to derive the cloud properties from these spectra. To analyze the data quantitatively, the mean and standard deviation of the retrieved parameters τ , f_i , $r_{e,w}$, and $r_{e,i}$ as well as the mean of the $1\text{-}\sigma$ error estimates, were computed for each ensemble. Comparing the mean retrieved value against the true value identifies any biases that may be induced by the physical retrieval. This approach was used to test the algorithm's sensitivity to different cloud optical depths, ice fractions, and sizes of the water and ice particles.

Of the four retrieved parameters, the one with the greatest information content in the spectrum is optical depth. The mean retrieved τ was within 2% of the true value of τ for all cases. For the other retrieved parameters, the differences between the mean values and

their true values were much more variable and a function of the cloud's optical depth.

Some of the simulation results are shown in Fig. 4. This figure is broken down into the results for water-only clouds (top), ice-only clouds (middle), and mixed-phase clouds (bottom). Five different optical depth bins were used—0.2, 0.5, 1.0, 2.0, and 4.0—and these bins are oriented along the x axis. Each panel shows the difference between the true value used in the simulation and the mean retrieved value, with the error bars denoting the ± 1 standard deviation of the mean retrieved value from the ensemble. The small x 's in Fig. 4 denote the size of the mean $1-\sigma$ error bar from the retrieval [Eq. (4)]. Comparing the mean $1-\sigma$ bars with the standard deviation from the ensemble illustrates how well the uncertainty in the retrieval is captured by the optimal estimation method, or, alternatively, how well the covariance matrix \mathbf{S}_e captures the covariance of the observations. For the single-phase clouds, different colors represent different true particle sizes, while in the mixed-phase clouds the different colors represent different ice fractions. For example, in the liquid-only clouds (Fig. 4a), the colors red, blue, green, and cyan are associated with the true effective radii of 5.5, 7.5, 9.5, and 11.5 μm , respectively.

One of the first conclusions is that the uncertainty in the retrieved particle sizes in the liquid- and ice-only clouds is larger for the smallest and largest optical depths ($\tau \geq 4$ or $\tau \leq 0.2$) than for intermediate values of τ ; this is because the spectral shape of the cloud emissivity becomes less pronounced as the emissivity nears either 0 or 1. The liquid water simulation results (Fig. 4a) indicate that the retrieval algorithm slightly underestimates the retrieved droplet size, with the size of the bias depending on droplet size and optical depth. This can be explained by considering the mixed-phase results in the Fig. 4c where the liquid-only clouds (red lines), which have a true $f_i = 0$, show that the retrievals are biased about 5%–20% high. The introduction of a small fraction of ice in these cases results in the underestimation of the size of the liquid water droplets by explaining some of the spectral signature with larger ice particles. This phenomenon becomes more pronounced as the liquid water droplets become larger, explaining why the underestimation of the size of the liquid water droplets increases with true droplet size (Fig. 4a).

The retrieved particle size of ice-phase clouds (Fig. 4b) does not show this bias, however, even though the retrieved f_i is often less than unity for these clouds (Fig. 4c). MIXCRA does underestimate the crystal size for crystals below 20 μm when $\tau \leq 0.5$. Interestingly, the physical retrieval is able to retrieve the crystal size in clouds with large crystals (45 and 70 μm , the latter is not shown) with some accuracy, especially when $\tau \geq 1$, although the uncertainty in these retrieved sizes is significant.

The skill of MIXCRA in retrieving the phase of the cloud is illustrated in Fig. 4c. In this panel, five different

ice fractions, corresponding to different colors, are used—0.0 (all liquid), 0.2, 0.5, 0.8, and 1.0 (all ice). The clouds have varying optical depths, but the effective radii of the particles are fixed to $r_{e,w} = 7.5 \mu\text{m}$ and $r_{e,i} = 21.5 \mu\text{m}$. As discussed earlier, the retrieved ice fraction is biased toward the center; that is, the algorithm tends to always want to include some ice and some liquid in each cloud, which is caused by the uncertainty in the emissivity observations between 400 and 600 cm^{-1} (which is primarily due to the uncertainty in PWV). This phenomenon is more pronounced when the cloud emissivity is near one of the extremes (i.e., small or large optical depth), where there is less information in the spectrum to separate the two phases. In general, however, the algorithm demonstrates good skill in determining the ice fraction of the cloud, and, hence, the phase.

The MIXCRA can easily be turned from a dual-phase retrieval to a single-phase retrieval by modifying the \mathbf{X}_a values in the parameter file. Several ice-only cloudy simulations were reprocessed with MIXCRA in the ice-only mode, and the results were compared with the MIXCRA dual-phase retrievals. Naturally, $f_i = 1.0$ for all values of τ in the ice-only retrieval, whereas it ranged from 0.84 to 0.97 for the dual-phase retrieval. The values of τ and $r_{e,i}$ were within 1% of their true values for the ice-only retrievals. Also, the $1-\sigma$ uncertainty in τ for the ice-only retrievals was 1/3–1/6 that of the dual-phase retrievals, and the $1-\sigma$ uncertainty in $r_{e,i}$ was about 1/2–1/3 as big. Similar results occurred when several liquid-only simulations were reprocessed with MIXCRA in the liquid-only mode. Again, the retrieved values of τ and $r_{e,w}$ were within 1% of their true values for the liquid-only retrieval. The $1-\sigma$ uncertainties were reduced 4–15 times for τ and 3–4 times for $r_{e,w}$. These large reductions in the uncertainties in τ and r_e result in much lower uncertainties in the derived IWP and LWP. Therefore, if accurate observations of the water path are required and there is a priori knowledge of the phase of the cloud, then this algorithm should be run in the single-phase mode.

5. Case studies

To evaluate the MIXCRA performance on real data, the MIXCRA results were compared with other retrieval methods in “simple” single-phase clouds. There are several techniques available to retrieve cloud properties in liquid-only and ice-only clouds, but there are relatively few techniques available for mixed-phase clouds. Some in situ data were collected via aircraft during FIRE ACE over the SHEBA site from May to June 1998 (Lawson et al. 2001), but most of those flights were in clouds that had optical depths above 5. The retrievals of mixed-phase properties from the millimeter-wave cloud radar (MMCR) and microwave radiom-

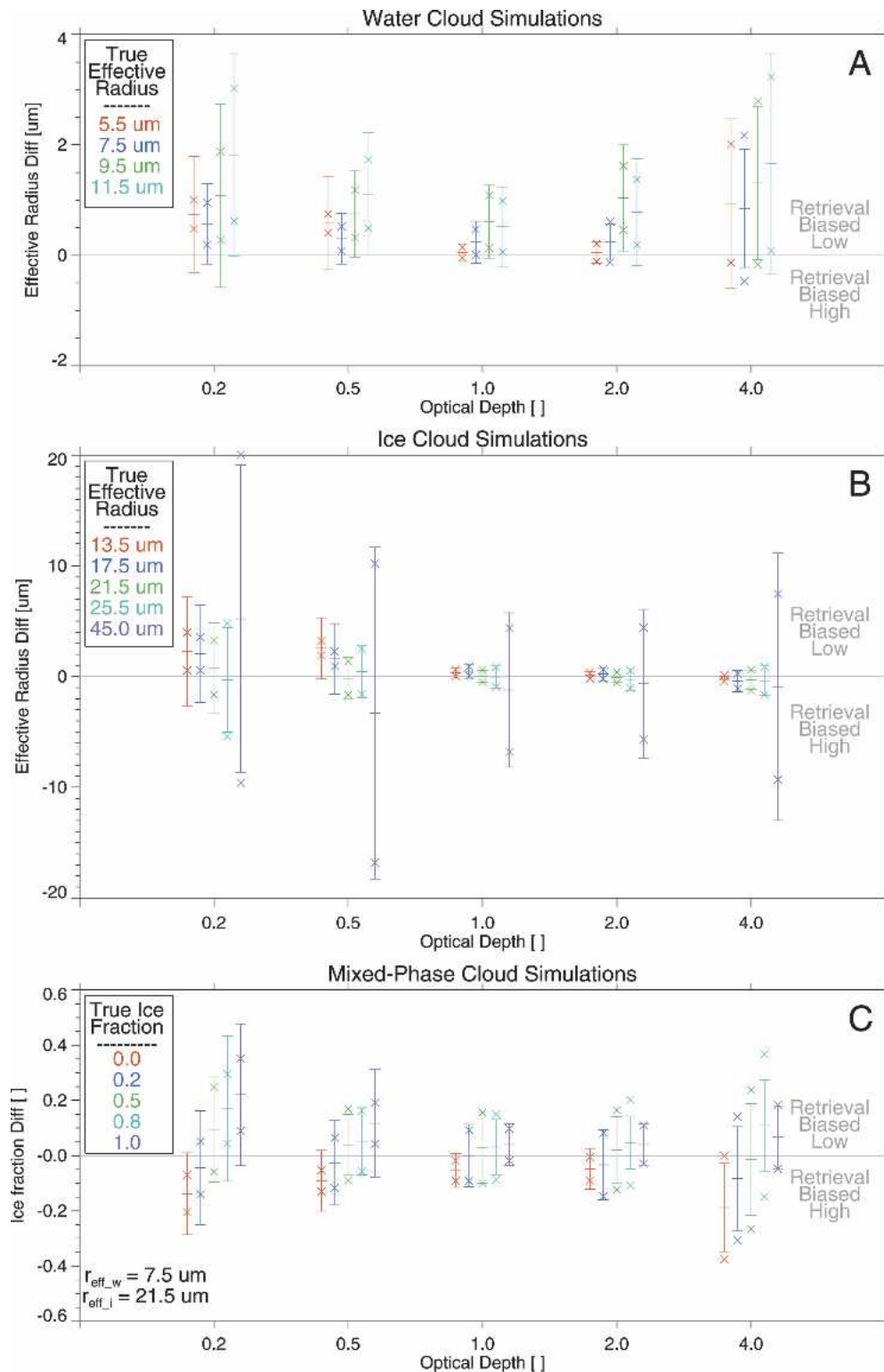


FIG. 4. Summary of the simulation testing results, showing the mean bias (center horizontal line) between the MIXCRA-retrieved values and truth. The error bars indicate the ± 1 standard deviation about the mean bias for the 60 samples in each cloud case. The "x"s denote the $\pm 1-\sigma$ range retrieved by the algorithm relative to the mean bias; values outside (inside) the error bars indicate that the retrieved $1-\sigma$ uncertainty overestimates (underestimates) the uncertainty in the retrieval. The plots are arranged as (a) all-liquid clouds, (b) all-ice clouds, and (c) mixed-phase clouds for the five optical depth "clusters" at $\tau = 0.2, 0.5, 1, 2$, and 4 .

eter (MWR) are promising (Shupe et al. 2001). However, Hobbs et al. (2001) have shown that in some cases the presence of only a few ice crystals in a liquid water cloud adds significant uncertainty in the radar-retrieved water content because of the sensitivity of the 35-GHz radar to large particles.

a. Liquid water cloud case study

Data collected on 15 May 1998 over the SHEBA ship were used to evaluate the liquid water retrievals from MIXCRA. From 2000 to 2400 UTC, a liquid water cloud existed above the ship that had an infrared emissivity less than unity. Several other groups (Lawson et al. 2001; Dong et al. 2001; Shupe et al. 2001) have studied this case, providing multiple datasets for comparison. The backscatter and depolarization ratio observed by the DABUL during this day are presented in Fig. 5. Note that during this period, a second cloud layer appeared between approximately 2000 and 2215 UTC. The low depolarization ratio ($<8\%$) observed by the lidar in the cloud layers from 2000 to 2400 UTC indicates that ice particles were not present.

The LWP and r_e results from MIXCRA for this period are shown in Fig. 5, with the error bars denoting the $1\text{-}\sigma$ uncertainty in the retrieved values. These results are compared against the standard statistical LWP retrievals that ARM provides from the brightness temperatures observed by the MWR (Liljegren and Lesht 1996). Also shown is the LWP that has been physically retrieved from the MWR data using an optimal estimation approach, where the forward model is a combination of the Rosenkranz water vapor and oxygen absorption models (Rosenkranz 1998) and Liebe et al. (1991) liquid water absorption model. Westwater et al. (2001) have suggested that using this absorption model combination results in more accurate PWV and LWP retrievals than do the absorption models that were used in the standard ARM retrievals. However, the uncertainty in the MWR retrievals is still approximately 25 g m^{-2} (Westwater et al. 2001). Dong et al. (2001) use the MWR-observed LWP (in this case from standard ARM retrievals) together with broadband solar flux observations and an iterative $\delta\text{-}2$ stream model to retrieve r_e ; these results are also shown. Retrievals from two different MMCR methods are also plotted for comparison. The Frisch et al. (1995) method uses the MWR to constrain the LWP, and by assuming that the droplet concentration and size distribution are constant with height, the effective radius can be retrieved from the MMCR's reflectivity. The absorption model used in the MWR retrievals for the Frisch method is the same model combination that was used in the physical microwave radiometer retrievals (T. Uttal 2002, personal communication). The Shupe et al. (2001) method is a MMCR reflectivity-based regression that is based upon aircraft observations during FIRE ACE. This method also assumes a constant number density and droplet

size distribution with altitude. Observations from an FSSP probe on the C-130 are also provided.

The comparison of the different methods to measure LWP shows good agreement between the AERI physical retrieval, the MWR physical retrieval, and the two radar methods (Fig. 5, Table 2). Note that this agreement is essentially unchanged by the presence of the second cloud layer from 2000 to 2215 UTC. There is considerable scatter in the FSSP observations of LWP, which makes them not very useful in this evaluation. The Dong et al. (2001) method does not retrieve LWP, but rather uses the MWR-retrieved value as a constraint to retrieve the effective radius of the droplets; that explains the agreement between Dong et al.'s results and the MWR statistical retrievals.

The retrieved droplet size for the MIXCRA and MMCR methods also show fair agreement, with the MIXCRA-retrieved r_e being slightly higher than that retrieved from the radar methods (Table 2). However, the MIXCRA results are biased low with respect to the aircraft in situ observations. The retrieved droplet size by the Dong et al. method overestimates the droplet size, but this bias may be caused by the overestimate of the LWP that resulted from using the statistically retrieved LWP from the MWR as the constraint.

b. Ice cloud case study

Several MMCR-based techniques have been applied to SHEBA data to retrieve both IWP and effective crystal size. The first technique (Matrosov 1999; henceforth called M99) is a radar-radiometer technique that uses a sky IR brightness temperature, which is calculated from the AERI at $11\text{ }\mu\text{m}$, to estimate the cloud optical depth. This optical depth is then used to constrain the retrieved ice water content (IWC) from the reflectivity observations. The IWC is then integrated over the cloud thickness to provide IWP. Then, using the Brown and Francis (1995) density-sized relationship, a characteristic particle size is determined. The visible optical depth is assumed to be twice the infrared optical depth that is derived from the AERI observations. This assumption, however, is only valid for certain particle sizes and depends on the ice crystal habit.

The second radar-based algorithm retrieves IWC from a reflectivity-based regression $\text{IWC} = aZ^b$, where the coefficients a and b are derived from other multi-measurement techniques and Z is the radar reflectivity (Shupe et al. 2004, manuscript submitted to *J. Appl. Meteor.*, henceforth referred to as the Shupe method). What distinguishes the Shupe method from other reflectivity-based retrievals is that the coefficient a varies as a function of season (M. Shupe 2003, personal communication). From these IWC retrievals, the IWP and particle size are determined as in the M99 method.

The third radar method (Matrosov et al. 2002; henceforth referred to as M02) uses the Doppler moments observed by the cloud radar. M02 is based upon a re-

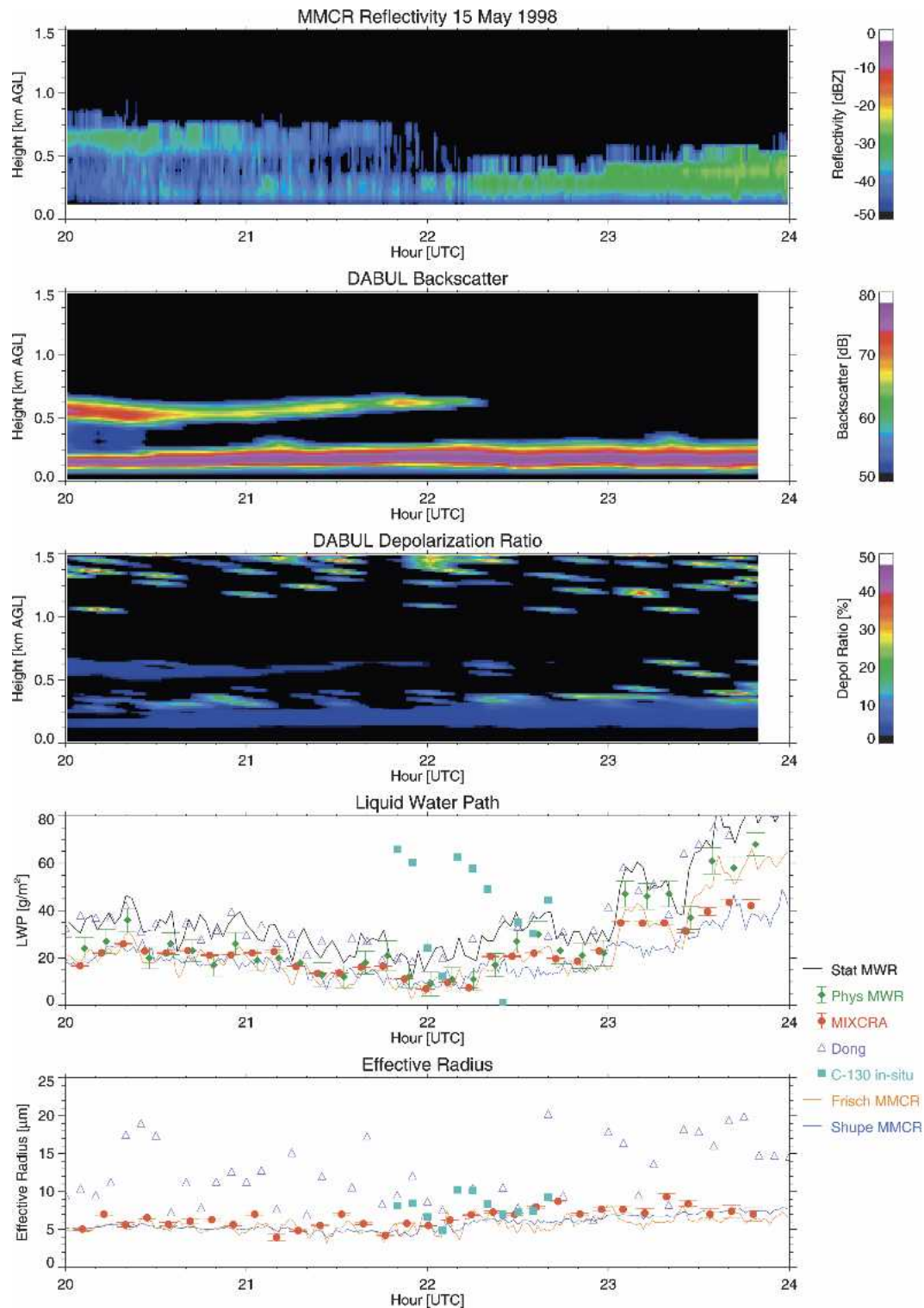


FIG. 5. (bottom two panels) Comparison of MIXCRA-retrieved liquid water path and liquid water droplet effective radius with other techniques for 15 May 1998 during SHEBA. (top three panels) The MMCR reflectivity and DABUL backscatter and depolarization are included for context. The results are summarized in Table 2. See text for details.

TABLE 2. Bias and root-mean-square (rms) differences in LWP and $r_{e,w}$ retrieved using MIXCRA and the other techniques for the 15 May 1998 case study from 2000 to 2400 UTC over the SHEBA site.

Technique	LWP bias (g m ⁻²)	LWP rms (g m ⁻²)	LWP correlation	$r_{e,w}$ bias (μm)	$r_{e,w}$ rms (μm)	$r_{e,w}$ correlation	<i>N</i>
Statistical MWR*	-14.6	16.5	0.95	Not available	Not available	Not available	32
Physical MWR**	-4.7	8.4	0.95	Not available	Not available	Not available	32
Dong	-15.3	17.6	0.89	-5.5	6.4	0.28	32
Frisch	-0.3	5.7	0.95	1.0	1.4	0.59	32
Shupe	3.2	5.1	0.91	0.8	1.2	0.70	32
C-130 FSSP	-25.9	34.5	-0.28	-1.3	2.0	0.26	11

*Standard ARM retrieval (Liljegren and Lesht 1996), which uses monthly retrieval coefficients developed from the Liebe and Layton (1987) absorption model for dry air and water vapor and the Grant et al. (1957) absorption model for liquid water.

** Physical iterative retrieval using the Rosenkranz (1998) absorption model for dry air and water vapor and the Liebe et al. (1991) absorption model for liquid water.

relationship between the particle fall speed, which is derived from the radar Doppler velocities, and the particle size. IWC is derived using the Brown and Francis (1995) relationship, but in the opposite sense as compared with the M99 technique. The IWC profile is then integrated to yield IWP. Profiles of extinction, which are integrated over the cloud thickness to yield the shortwave optical depth, are computed following Matrosov et al. (2002).

It should be noted that the effective diameter D_e that is used for the radar retrievals follows the definition from Mitchell (2002), which is defined as

$$D_e = \frac{1.5\text{IWC}}{\rho_i A}, \quad (10)$$

where ρ_i is the bulk density of ice and A is the total projected area of the crystals. The total projected area is taken to be one-half of the visible extinction coefficient, which is computed from the visible optical depth. The effective radius is then $D_e/2$. However, this formulation of effective radius is much different than the formulation used in MIXCRA, which is the ratio of the third moment to the second moment of the size distribution. Therefore, to overcome the different formulations of effective ice particle size, we examine the ratio of the IWP to cloud optical depth (Comstock et al. 2004).

A comparison between these three MMCR-based methods and the MIXCRA technique for 28 April 1998 is shown in Fig. 6. The MIXCRA retrieval was performed twice—once where the ice particles were assumed to be spheres and once assuming that the ice habit was the droxtal-hexcolumns model. There is significant spread between the MMCR retrievals of IWP, with the M02 results having a factor of 2–3 times more ice mass than the Shupe results, and the M99 results falling between these two. [However, other SHEBA case studies show different relative orderings of the three MMCR algorithms (e.g., Turner 2003).] The MIXCRA results demonstrate that the IWP that is retrieved using the droxtal-hexcolumn habit model is approximately twice that of the retrieved IWP when the

ice is modeled as a sphere; this relationship is fairly consistent across many case studies. The droxtal-hexcolumn retrievals track with the M99 results, and the spherical IWP retrievals are in fair qualitative agreement with the Shupe reflectivity technique.

While there is large variability in the MMCR-based IWP results shown in Fig. 6, the same amount of variability is also demonstrated at the Southern Great Plains (SGP) Cloud and Radiation Test Bed (CART) site (e.g., Sassen and Mace 2002; Comstock et al. 2004). Also, the retrievals at the SGP site demonstrate that they bracket in situ observations made by aircraft fairly well (J. Mace 2002, personal communication). In any regard, infrared retrievals of IWP are very sensitive to ice particle habit, and thus large uncertainties in IWP will exist unless the habit of the cloud can be retrieved or accurately specified. The retrieval of ice habit from the remote sensing data is beyond the scope of this work.

6. SHEBA results

The SHEBA campaign started in October 1997 and wrapped up in early September 1998. During this period, the AERI operated normally from late October to mid-May. MIXCRA was applied to these data; only data for which the cloud emissivity at 900 cm⁻¹ was between 0.05 and 0.95, for which the AERI's hatch (which protects the instrument's fore optics from precipitation) was open, for which the final root-mean-square difference between the observed and calculated emissivity was below 0.060 (as a measure of convergence), and for which the uncertainty in the effective cloud temperature was less than 3 K were analyzed here. This last restriction ensures that only single-layer clouds are included in the analysis. The number of valid retrievals per month from 1 November 1997 through 21 May 1998 was 1311, 817, 604, 384, 1205, 1391, and 745, respectively. The decrease in the number of samples in December and January is due to the increased occurrence of clear skies, because these months were the least cloudy during the SHEBA campaign (Intrieri et

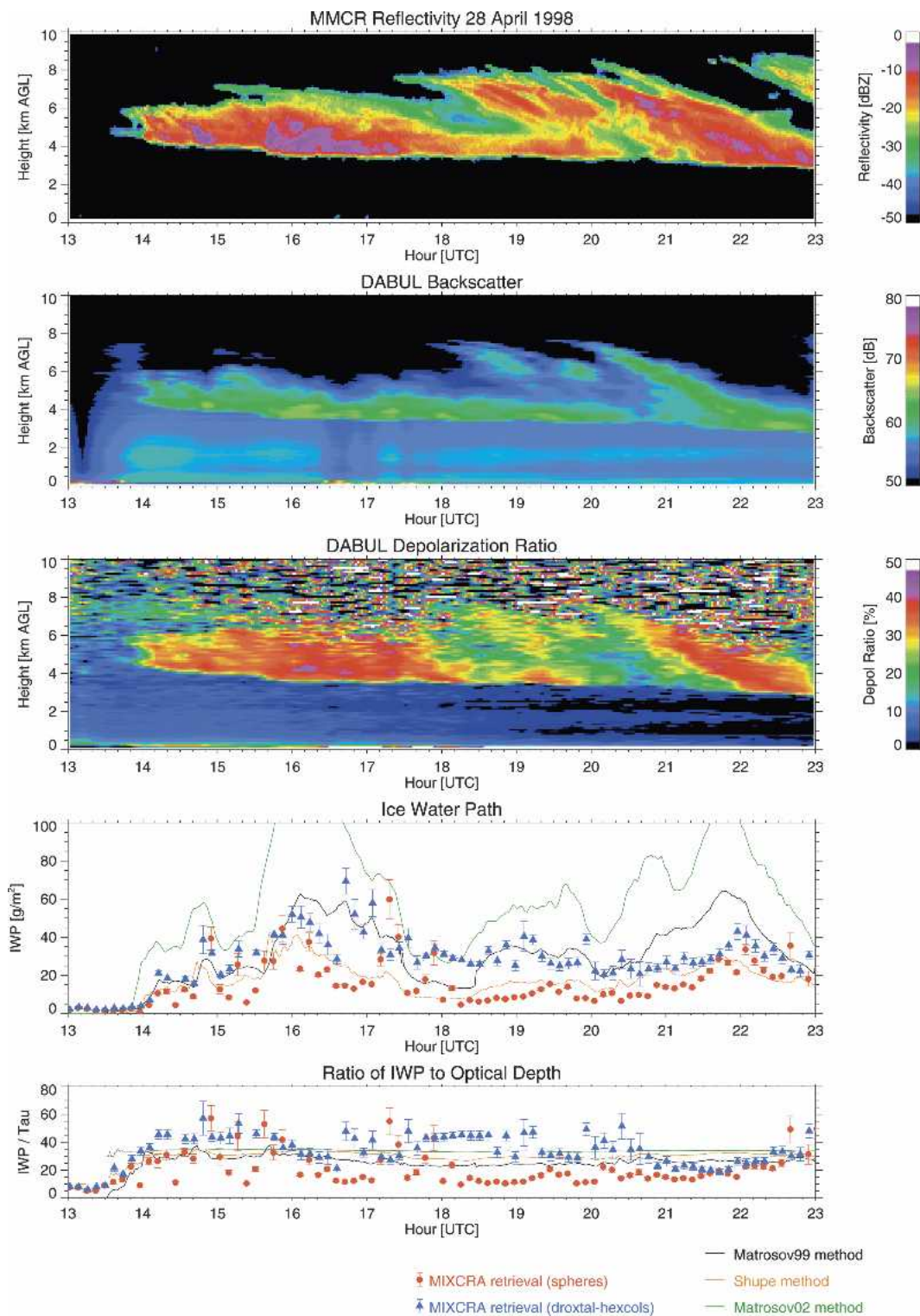


FIG. 6. (bottom two panels) Comparison of MIXCRA-retrieved ice water path and ice particle size with other retrieval techniques for 28 Apr 1998 during SHEBA. (top three panels) The MMCR reflectivity and DABUL backscatter and depolarization are included for context. See text for details.

al. 2002). The DABUL's laser required maintenance during February, which explains the decreased number of cloud samples in that month.

An example showing the results from the retrieval algorithm is shown in Fig. 7. Two distinct cloud layers are present on this day: a high cirrus layer from approximately 0600 to 1800 UTC, and a midlevel cloud from 1800 to 2300 UTC. For the cirrus cloud, the effective cloud temperature is below -40°C , and, thus, MIXCRA switched automatically into single-phase mode. Note that the optical depths associated with the cirrus cloud are quite small (less than 0.2). The retrieved particle size for this cirrus cloud ranged from 10 to $60\text{ }\mu\text{m}$ and appears to be correlated with the altitude and/or thickness of the cirrus cloud.

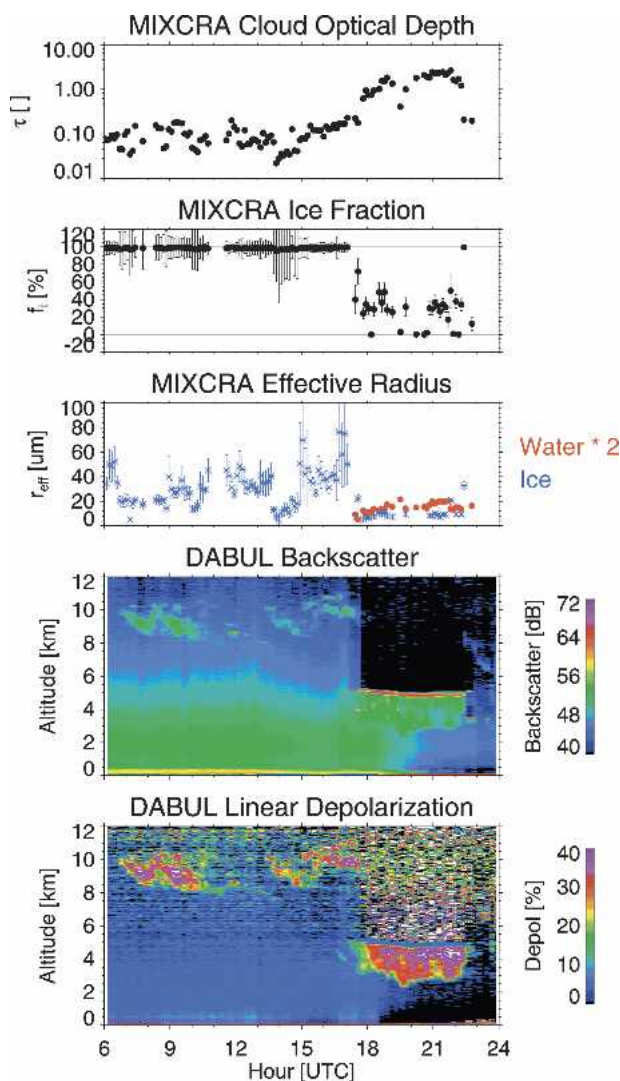


FIG. 7. Example of the MIXCRA-retrieved cloud properties (top three panels) cloud optical depth, ice fraction, and effective radii of the water and ice particles for 8 Mar 1998 during SHEBA. (bottom two panels) The DABUL backscatter and depolarization ratio are also shown. See text for details.

The midlevel cloud in Fig. 7 has significantly higher optical depths (as retrieved using MIXCRA), with a maximum optical depth approaching 2. The DABUL data demonstrate that there is a layer with high backscatter values at the top of the cloud near 5 km and the depolarization ratio associated with this layer is less than 10%; this layer is most likely composed of mostly liquid water droplets. However, below this geometrically thin layer is a much thicker (geometrically) layer that extends down to approximately 3 km. This layer has much lower backscatter values than the layer at the top of the cloud, and the depolarization values are around 30%, indicating that this layer contains ice crystals. The vertical structure of a geometrically thin liquid water layer over a thicker ice layer is predicted by models (e.g., Jiang et al. 2000; Girard and Blanchet 2001) and noted in observations (e.g., Pinto 1998; Lawson et al. 2001) of Arctic clouds. The MIXCRA-retrieved ice fraction varied from zero to near 40% for this midlevel cloud. The retrieved effective radius for the water droplets ranged from 5 to $10\text{ }\mu\text{m}$ (note that these values were multiplied by 2 on the figure) and the retrieved effective radius for the ice particles was approximately $10\text{ }\mu\text{m}$ for the midlevel cloud.

Figure 8 shows the distribution of the retrieved optical depth (Fig. 8b) and ice fraction (Fig. 8d) for the single-layer optically thin clouds during 7-month SHEBA period (November through May). There is a relative increase in the number of clouds with $\tau < 0.5$; these are predominantly ice-only clouds. The decline in the number of clouds with optical depths above 5 is partially due to the infrared emissivity upper threshold value of 0.95, which corresponds to an optical depth between 4 and 6, depending on the phase and size of the cloud particles. Using ice fraction threshold values of 10% and 90% for liquid- and ice-only clouds, these single-layer clouds were liquid only, mixed phase, or ice only 20%, 48%, and 32% of the time, respectively. Note that the mode value of the ice fraction distribution for mixed-phase clouds is about 35%, implying that the majority of the optical depth in these mixed-phase clouds is associated with the liquid water, not the ice.

Figure 8 also shows the optical depth and ice fraction as a function of the cloud temperature (Figs. 8a and 8c, respectively). The optical depth data (Fig. 8a) show a slight correlation with temperature for low optical depths. Figure 8c shows that a significant number of liquid and mixed-phase clouds exist at temperatures as low as 240 K. However, there is no general trend in the retrieved ice fraction with increasing temperature, unlike the somewhat better defined relationship shown in Gregory and Morris (1996) that was derived from mid-latitude frontal cloud observations. This suggests that cloud temperature is not a good proxy to use to determine Arctic cloud phase in global climate models.

The effective particle size is important for the determination of the total water content of the cloud and for radiative transfer calculations. The distributions of the

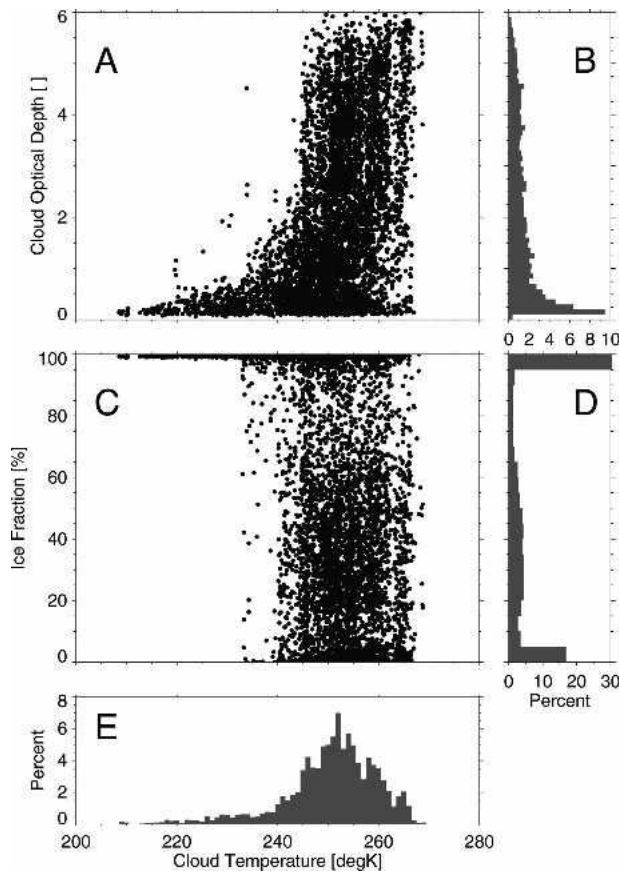


FIG. 8. Frequency distributions of (b) cloud optical depth, (d) ice fraction, and (e) cloud temperature, along with scatterplots of (a) optical depth and (c) ice fraction as a function of cloud temperature, retrieved by MIXCRA from single-layer optically thin clouds from 1 Nov 1997 to 21 May 1998 at SHEBA. There are 6457 cloudy samples in this dataset.

retrieved effective radii ($r_{e,w}$) for the water droplets in both liquid-only and mixed-phase clouds are shown in Fig. 9 (middle row). The mode values of the distribution of $r_{e,w}$ for the liquid-only and mixed-phase clouds are approximately 10 and 7 μm , respectively. There are also more cases with large $r_{e,w}$ in the single-phase liquid clouds than in the mixed-phase clouds. The lack of the larger water droplets in the mixed-phase clouds, which results in a shift to a smaller effective radius, may be due to the larger droplets being removed from the size distribution because the larger droplets are more likely to freeze (Rangno and Hobbs 2001). It should be noted that drizzle droplets have significantly larger effective radii ($>30 \mu\text{m}$), but when drizzle conditions occur the cloud is typically opaque in the infrared, and these cases were, thus, screened out of the dataset.

The distributions of the retrieved ice particle sizes ($r_{e,i}$) for mixed-phase and ice-only clouds are also shown in Fig. 9 (bottom row). The distribution of $r_{e,i}$ for ice-only clouds shows a mode radius of approximately 25 μm with a significant number of cases with larger

effective radii. However, the mode of the distribution of $r_{e,i}$ for mixed-phase clouds is approximately 10 μm , and there are relatively few cases where the retrieved $r_{e,i}$ was larger than 50 μm in a mixed-phase cloud. This result appears inconsistent: one might expect ice particles to grow rapidly to a large size (much larger than 10 μm) in the presence of large amounts of supercooled liquid water and, thus, the effective radius of these ice particles should be much larger. A variety of simulations were performed (in the spirit of section 4) to determine if these small ice particles in mixed-phase clouds were an artifact of the retrieval. The simulations covered a wide range of optical depths and particle sizes. The simulations demonstrated that the MIXCRA-retrieved values of τ , f_i , and $r_{e,w}$ show relatively little bias, but that the retrieved $r_{e,i}$ often is biased a bit low. For example, for a simulated cloud with $\tau = 3$, $f_i = 0.3$, $r_{e,w} = 9 \mu\text{m}$, and $r_{e,i} = 40 \mu\text{m}$, the mean retrieved value for $r_{e,i}$ was $30.6 \pm 11.0 \mu\text{m}$ (the standard deviation is computed about the mean of the 60 instances of this cloud as in section 4). This example is a worst-case scenario, because both the optical depth and the ice particle size are near the upper ends of their respective sensitivity ranges in the infrared; in general, the bias in the retrieved $r_{e,i}$ was much smaller. Therefore, the apparent inconsistency in the retrieved $r_{e,i}$ in mixed-phase clouds (i.e., that the retrieved crystal size is small) does not appear to be an artifact of the retrieval.

The underlying assumption in the previous paragraph is that the ice habit (and, thus, single scattering properties) used in MIXCRA is representative of the shape of the ice particles in the overhead clouds. The effective radius is essentially the ratio of the volume to the projected area of the crystal; therefore, if the ice particles were growing in a manner such that the surface area was increasing faster than the volume (such as by riming or aggregation) then the effective radius would decrease. However, simulations of Arctic clouds suggest that ice crystals grow by vapor deposition and that collision-coalescence plays a much smaller role in ice crystal growth (Harrington et al. 1999, Girard and Blanchet 2001), making the hypothesis of the projected area growing faster than volume less likely. Alternatively, Grenfell and Warren (1999) and Neshyba et al. (2003) have demonstrated that a larger number of smaller crystals with the same volume/area ratio (i.e., “equivalent” crystals) as the original crystal distribution can accurately match the radiative properties of the original crystal distribution. As a result, if the assumed ice habit is not accurate, then the retrieval may match the radiative properties by using equivalent crystals of the assumed habit (spheres or droxtal-hexcolumns), which result in smaller effective radii and a higher number density than the cloud’s true ice crystal distribution. Therefore, the difference in the distribution of $r_{e,i}$ for ice-only and mixed-phase clouds during SHEBA suggests that the shape of the ice particles in the mixed-

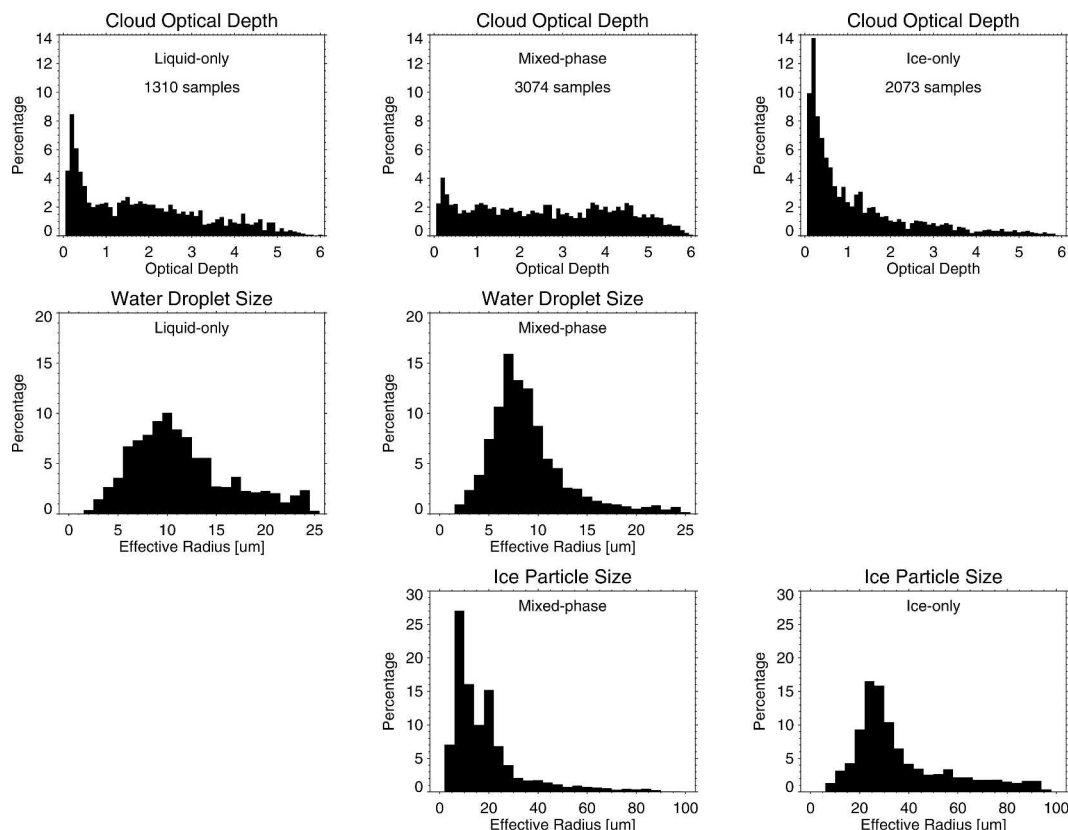


FIG. 9. (top) Distribution of cloud optical depth and effective radii for (middle) water droplets and (bottom) ice particles for (left) liquid-only, (center) mixed-phase, and (right) ice-only clouds during SHEBA. The ice fraction thresholds used to separate liquid-only, mixed-phase, and ice-only clouds were 10% and 90%, respectively.

phase clouds is significantly different than the shape of the ice particles in ice-only clouds.

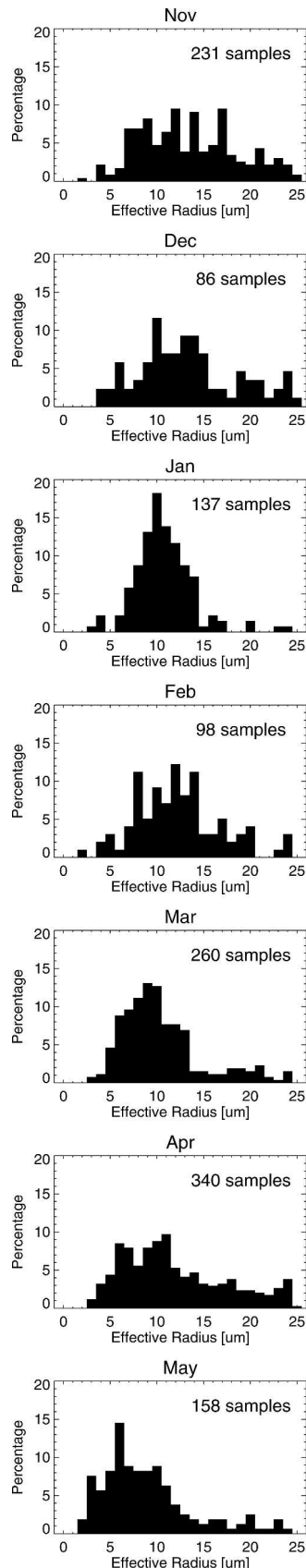
The AERI data collected during SHEBA spanned across the winter to late spring, and, thus, it is possible to look for any changes in the cloud properties that are associated with the changing seasons. The winter months have the coldest and thinnest clouds, and the clouds tend to become thicker and warmer in the spring. Significant numbers of liquid-phase and mixed-phase clouds exist throughout the winter, making up well over half of the clouds from January through May. Surprisingly, the relative distribution of the ice fraction was unchanged from January through May, even though the clouds are becoming increasingly warmer over this time period.

The distribution of droplet effective radius in liquid-only clouds ($f_i < 10\%$) is shown in Fig. 10. The distribution of $r_{e,w}$ shows that the mode value of the distribution is approximately $10 \mu\text{m}$ in the winter months, and shifts to $7 \mu\text{m}$ by May. The mode value of approximately $7 \mu\text{m}$ in May agrees well with April–July mean $r_{e,w}$ value at SHEBA reported by Shupe et al. (2001) and the average May 2000 value at the ARM NSA site (Dong and Mace 2003). The decrease in droplet size from the winter to spring may be associated with the

increase in anthropogenic aerosols advected to the Arctic from the midlatitudes (Barrie and Hoff 1986; Sirois and Barrie 1999).

7. Summary

A mixed-phase cloud property retrieval algorithm (MIXCRA), which uses the physical iterative optimal estimation approach, was developed to retrieve cloud optical depth, ice fraction, liquid and ice water paths, and the effective radius of the water droplets and ice particles from single-layer optically thin clouds using data from ground-based AERI radiance and lidar cloud boundary observations. Simulated data and case studies were used to characterize this retrieval algorithm. The case studies demonstrated good agreement between the MIXCRA results and other retrieval methods in liquid water path (mean differences of $\pm 5 \text{ g m}^{-2}$) and effective radius of the water droplets (mean differences of $\pm 1.3 \mu\text{m}$) for a liquid-only cloud, and fair agreement among the retrieval methods was shown in the retrieved ice water path for ice clouds. The simulation studies demonstrated that the algorithm is most sensitive to errors in the PWV and cloud temperature. The retrieved ice fraction is slightly biased toward mixed-phase clouds in many cases because of the uncertainty



in the 17–25- μm cloud emissivity observations, which results from the uncertainty in the PWV that was used in the emissivity calculation. The optical depth and ice fraction are insensitive to the ice habit that was used in the retrieval; however, the use of different ice habit distributions resulted in significantly different ice water path values.

MIXCRA was used to retrieve microphysical cloud properties from AERI and DABUL observations from 1 November 1997 to 21 May 1998 above the SHEBA camp. This retrieval is only applicable during single-layer optically thin ($\tau < 6$) cases where the PWV is less than 1 cm; during this period, 63% of the cloudy scenes satisfied these conditions. Many details about the microphysical properties of the clouds over the SHEBA camp were illuminated by this dataset. This analysis showed that the single-layer optically thin clouds were mixed phase, liquid only, and ice only approximately 48%, 20%, and 32% of the time, respectively. Clouds with optical depths less than 0.5 were predominantly ice clouds. There was no clear relationship between the ice fraction and the cloud temperature. The retrieved water droplet effective radius in mixed-phase clouds was, in general, smaller than the retrieved effective radius in a liquid-only cloud. The retrieved ice particle effective radius in mixed-phase clouds was significantly smaller than that retrieved in ice-only clouds; we suggest that this is due to differences in the ice habit in mixed-phase clouds relative to ice-only clouds. Detailed in situ analysis of the shape of the ice particles in mixed-phase and ice-only clouds during the Mixed-Phase Arctic Cloud Experiment (M-PACE) at the ARM NSA site in October 2004 will be used to investigate this hypothesis (see further information about M-PACE online at <http://www.db.arm.gov/cgi-bin/IOP/iops.pl>). Last, the distribution of droplet effective radius in liquid-only clouds shifts from a mode value of approximately 10 μm in the winter to 7 μm in the late spring; analysis of the longer time series of data at the ARM NSA site, in conjunction with the in situ aerosol observations made by the collocated NOAA Climate Monitoring and Diagnostics Laboratory (CMDL), will be used to investigate the hypothesis that the changing droplet size is correlated with the aerosol number concentration.

The MIXCRA technique provides a promising new tool in the cloud microphysical property retrieval arsenal, because there are very limited ways to observe microphysical properties in mixed-phase clouds. The sensitivity of this AERI-based retrieval algorithm to optically thin clouds complements other retrieval techniques that rely on LWP observations from the MWR (e.g., Shupe et al. 2001), which are more applicable and have less uncertainty when the LWPs are above 50 g

←

FIG. 10. Distribution of retrieved water droplet effective radii in liquid-only clouds per month during SHEBA.

m^{-2} . While the ability to retrieve cloud phase requires that the PWV be less than 1 cm so that the 16–25- μm window is semitransparent, MIXCRA can be operated in a single-phase mode (i.e., by specifying the cloud phase via X_a in the retrieval) to retrieve cloud properties from single-layer clouds in conditions where the PWV is larger than 1 cm. Therefore, this algorithm can also be used to investigate the microphysical properties of optically thin stratus clouds or cirrus clouds at mid-latitude or tropical sites.

Acknowledgments. This research was funded by the Department of Energy's Atmospheric Radiation Measurement (ARM) Program. The DABUL data used in this analysis were provided by Janet Intrieri, and the radiosonde and MMCR reflectivity data were acquired from the University Corporation for Atmospheric Research (UCAR) Joint Office for Scientific Support (JOSS) archive. The author gratefully acknowledges the contributions of Matthew Shupe and Xiquan Dong, who provided the MMCR-based and solar broadband retrieval datasets for the case studies. Discussions with Steve Ackerman, Bryan Baum, Ken Sassen, and two anonymous reviewers significantly improved this paper.

REFERENCES

- Alvarez, R. J., W. L. Eberhard, J. M. Intrieri, C. J. Grund, and S. P. Sandberg, 1998: A depolarization and backscatter lidar for unattended operation in varied meteorological conditions. *Proc. 10th Symp. on Meteorological Observations and Instrumentation*, Phoenix, AZ, Amer. Meteor. Soc., 140–144.
- Barrie, L. A., and R. M. Hoff, 1986: Five years of air chemistry observations in the Canadian Arctic. *Atmos. Environ.*, **19**, 1995–2010.
- Bevington, P. R., and D. K. Robinson, 1992: *Data Reduction and Error Analysis for the Physical Sciences*. McGraw-Hill, 328 pp.
- Brown, P. R. A., and P. N. Francis, 1995: Improved measurements of the ice water content in cirrus using a total-water probe. *J. Atmos. Oceanic Technol.*, **12**, 410–414.
- Clough, S. A., and M. J. Iacono, 1995: Line-by-line calculations of atmospheric fluxes and cooling rates: Application to carbon dioxide, ozone, methane, nitrous oxide, and the halocarbons. *J. Geophys. Res.*, **100**, 16 519–16 535.
- Comstock, J. M., and Coauthors, 2004: High clouds microphysical retrievals intercomparison. *Proc. 14th Atmospheric Radiation Measurement (ARM) Program Science Team Meeting*, Albuquerque, NM, U.S. Dept. of Energy. [Available online at http://www.arm.gov/publications/proceedings/conf14/extended_abs/comstock-jm.pdf.]
- Curry, J. A., W. B. Rossow, D. Randall, and J. L. Schramm, 1996: Overview of Arctic cloud and radiation characteristics. *J. Climate*, **9**, 1731–1764.
- Daniel, J. S., S. Solomon, R. W. Portmann, A. O. Langford, C. S. Eubank, E. G. Dutton, and W. Madeson, 2002: Cloud liquid water and ice measurements from spectrally resolved near-infrared observations: A new technique. *J. Geophys. Res.*, **107**, 4599, doi:10.1029/2001JD000688.
- DeSlover, D. H., W. L. Smith, P. K. Piironen, and E. W. Eloranta, 1999: A methodology for measuring cirrus cloud visible-to-infrared spectral optical depth ratios. *J. Atmos. Oceanic Technol.*, **16**, 251–262.
- Dong, X., and G. G. Mace, 2003: Arctic stratus cloud properties and radiative forcing at the ARM NSA site. *J. Climate*, **16**, 445–461.
- , —, P. Minnis, and D. F. Young, 2001: Arctic stratus cloud properties and their effect on the surface radiation budget: Selected cases from FIRE ACE. *J. Geophys. Res.*, **106**, 15 297–15 312.
- Downing, H. D., and D. Williams, 1975: Optical constants of water in the infrared. *J. Geophys. Res.*, **80**, 1656–1661.
- Frisch, A. S., C. W. Fairall, and J. B. Snider, 1995: Measurements of stratus cloud and drizzle parameters in ASTEX with a Ka-band Doppler radar and microwave radiometer. *J. Atmos. Sci.*, **52**, 2788–2799.
- Girard, E., and J.-P. Blanchet, 2001: Simulation of Arctic diamond dust, ice fog, and thin stratus using an explicit aerosol–cloud–radiation model. *J. Atmos. Sci.*, **58**, 1199–1221.
- Grant, E. H., J. Buchanan, and H. F. Cook, 1957: Dielectric behavior of water at microwave frequencies. *J. Chem. Phys.*, **26**, 641–651.
- Gregory, D., and D. Morris, 1996: The sensitivity to climate simulations to the specification of mixed phase clouds. *Climate Dyn.*, **12**, 641–651.
- Grenfell, T. C., and S. G. Warren, 1999: Representation of a non-spherical ice particle by a collection of independent spheres for scattering and absorption of radiation. *J. Geophys. Res.*, **104**, 31 697–31 709.
- Harrington, J. Y., T. Reisin, W. R. Cotton, and S. M. Kreidenweis, 1999: Cloud resolving simulations of Arctic stratus. Part II: Transition-season clouds. *Atmos. Res.*, **51**, 45–75.
- Herman, G. F., 1980: Thermal radiation in Arctic stratus clouds. *Quart. J. Roy. Meteor. Soc.*, **106**, 771–780.
- Hobbs, P. V., A. L. Rangno, M. Shupe, and T. Uttal, 2001: Airborne studies of cloud structures over the Arctic Ocean and comparisons with retrievals from ship-based remote sensing measurements. *J. Geophys. Res.*, **106**, 15 029–15 044.
- Houghton, J. T., B. A. Callander, and S. V. Varney, Eds., 1992: *Climate Change 1992: The Supplementary Report of the IPCC Scientific Assessment*. Cambridge University Press, 200 pp.
- Intrieri, J. M., M. D. Shupe, T. Uttal, and B. J. McCarty, 2002: An annual cycle of Arctic cloud characteristics observed by radar and lidar at SHEBA. *J. Geophys. Res.*, **107**, 8030, doi:10.1029/2000JC000423.
- Jiang, H., W. R. Cotton, J. O. Pinto, J. A. Curry, and M. J. Weisbluth, 2000: Cloud resolving simulations of a mixed-phase Arctic stratus observed during BASE: Sensitivity to concentration of ice crystals and large-scale heat and moisture advection. *J. Atmos. Sci.*, **57**, 2105–2117.
- Knuteson, R. O., and Coauthors, 2004: Atmospheric Emitted Radiance Interferometer (AERI). Part I: Instrument design. *J. Atmos. Oceanic Technol.*, **21**, 1763–1776.
- Lawson, R. P., B. A. Baker, C. G. Schmitt, and T. L. Jensen, 2001: An overview of microphysical properties of Arctic clouds observed in May and July 1998 during FIRE.ACE. *J. Geophys. Res.*, **106**, 14 989–15 014.
- Liebe, H. J., and D. H. Layton, 1987: Millimeter wave properties of the atmosphere: Laboratory studies and propagation modeling. National Telecommunications and Information Administration Rep. 87-24, 74 pp.
- , G. A. Hufford, and T. Manabe, 1991: A model for the complex permittivity of water at frequencies below 1 THz. *Int. J. Infrared Millimeter Waves*, **12**, 659–675.
- Liljegren, J. C., and B. M. Lesht, 1996: Measurements of integrated water vapor and cloud liquid water from microwave radiometers at the DOE ARM cloud and radiation testbed in the U.S. southern Great Plains. *Proc. Int. Geoscience and Remote Sensing Symp. (IGARSS)*, Lincoln, NB, IEEE, 1675–1677.
- Marty, C., and Coauthors, 2003: Downward longwave irradiance uncertainty under Arctic atmospheres: Measurements and modeling. *J. Geophys. Res.*, **108**, 4358, doi:10.1029/2002JD002937.

- Matrosov, S. Y., 1999: Retrievals of vertical profiles of ice cloud microphysics from radar and IR measurements using tuned regressions between reflectivity and cloud parameters. *J. Geophys. Res.*, **104**, 16 741–16 753.
- , A. V. Korolev, and A. J. Heymsfield, 2002: Profiling cloud ice mass and particle characteristic size from Doppler radar measurements. *J. Atmos. Oceanic Technol.*, **19**, 1003–1018.
- Minnett, P. J., R. O. Knuteson, F. A. Best, B. J. Osborne, J. A. Hanafin, and O. B. Brown, 2001: The marine-atmospheric emitted radiance interferometer: A high-accuracy, seagoing infrared spectrometer. *J. Atmos. Oceanic Technol.*, **18**, 994–1013.
- Mitchell, D. L., 2002: Effective diameter in radiation transfer: General definition, applications, and limitations. *J. Atmos. Sci.*, **59**, 2330–2346.
- Neshyba, S. P., T. C. Grenfell, and S. G. Warren, 2003: Representation of a nonspherical ice particle by a collection of independent spheres for scattering and absorption of radiation: 2. Hexagonal columns and plates. *J. Geophys. Res.*, **108**, 4448, doi:10.1029/2002JD003302.
- Pinto, J. O., 1998: Autumnal mixed-phase cloudy boundary layers in the Arctic. *J. Atmos. Sci.*, **55**, 2016–2038.
- Rangno, A. L., and P. V. Hobbs, 2001: Ice particles in stratiform clouds in the Arctic and possible mechanisms for the production of high ice concentrations. *J. Geophys. Res.*, **106**, 15 065–15 075.
- Rodgers, C. D., 2000: *Inverse Methods for Atmospheric Sounding*. World Scientific, 238 pp.
- Rosenkranz, P. W., 1998: Water vapor microwave continuum absorption: A comparison between measurements and models. *Radio Sci.*, **33**, 919–928.
- Sassen, K., and J. M. Comstock, 2001: A midlatitude cirrus cloud climatology from the Facility for Atmospheric Remote Sensing. Part III: Radiative properties. *J. Atmos. Sci.*, **58**, 2113–2127.
- , and G. G. Mace, 2002: Ground-based remote sensing of cirrus clouds. *Cirrus*, D. K. Lynch et al., Eds., Oxford University Press, 168–195.
- Shupe, M. D., T. Uttal, S. Y. Matrosov, and A. S. Frisch, 2001: Cloud water contents and hydrometeor sizes during the FIRE-Arctic Clouds Experiment. *J. Geophys. Res.*, **106**, 15 015–15 028.
- Sirois, A., and L. A. Barrie, 1999: Arctic lower tropospheric aerosol trends and composition at Alert, Canada: 1980–1995. *J. Geophys. Res.*, **104**, 11 599–11 618.
- Smith, W. L., X. L. Ma, S. A. Ackerman, H. E. Revercomb, and R. O. Knuteson, 1993: Remote sensing cloud properties from high spectral resolution infrared observations. *J. Atmos. Sci.*, **50**, 1708–1720.
- , W. F. Feltz, R. O. Knuteson, H. E. Revercomb, H. M. Woolf, and H. B. Howell, 1999: The retrieval of planetary boundary layer structure using ground-based infrared spectral radiance measurements. *J. Atmos. Oceanic Technol.*, **16**, 323–333.
- Stamnes, K., S.-C. Tsay, W. Wiscombe, and K. Jayaweera, 1988: A numerically stable algorithm for discrete-ordinate-method radiative transfer in multiple scattering and emitting layered media. *Appl. Opt.*, **27**, 2502–2509.
- , R. G. Ellingson, J. A. Curry, J. E. Walsh, and B. D. Zak, 1999: Review of science issues, deployment strategy, and status of the ARM North Slope of Alaska–Adjacent Arctic Ocean climate research site. *J. Climate*, **12**, 46–63.
- Stephens, G. L., 1994: *Remote Sensing of the Lower Atmosphere: An Introduction*. Oxford University Press, 523 pp.
- Sun, Z., and K. P. Shine, 1995: Parameterization of ice cloud radiative properties and its application to the potential climatic importance of mixed-phase clouds. *J. Climate*, **8**, 1874–1888.
- Turner, D. D., 2003: Microphysical properties of single and mixed-phase Arctic clouds derived from ground-based AERI observations. Ph.D. thesis, University of Wisconsin—Madison, 167 pp. [Available online at <http://www.ssec.wisc.edu/library/turnerdissertation.pdf>.]
- , S. A. Ackerman, B. A. Baum, H. E. Revercomb, and P. Yang, 2003: Cloud phase determination using ground-based AERI observations at SHEBA. *J. Appl. Meteor.*, **42**, 701–715.
- , and Coauthors, 2004: The QME AERI LBLRTM: A closure experiment for downwelling high spectral resolution infrared radiance. *J. Atmos. Sci.*, **61**, 2657–2675.
- Uttal, T., and Coauthors, 2002: Surface heat budget of the Arctic Ocean. *Bull. Amer. Meteor. Soc.*, **83**, 255–275.
- Warren, S., 1984: Optical constants of ice from the ultraviolet to the microwave. *Appl. Opt.*, **23**, 1206–1225.
- Westwater, E. R., Y. Han, M. D. Shupe, and S. Y. Matrosov, 2001: Analysis of integrated cloud liquid and precipitable water vapor retrievals from microwave radiometers during the Surface Heat Budget of the Arctic Ocean Project. *J. Geophys. Res.*, **106**, 32 019–32 030.
- Wiscombe, W. J., 1980: Improved Mie scattering algorithms. *Appl. Opt.*, **19**, 1505–1509.
- Yang, P., B. C. Gao, B. A. Baum, Y. X. Hu, W. J. Wiscombe, S. C. Tsay, D. M. Winker, and S. L. Nasiri, 2001: Radiative properties of cirrus clouds in the infrared (8–13 μm) spectral region. *J. Quant. Spectrosc. Radiat. Transfer*, **70**, 473–504.
- , B. A. Baum, A. J. Heymsfield, Y. X. Hu, H.-L. Huang, S.-C. Tsay, and S. A. Ackerman, 2003: Single-scattering properties of droxtals. *J. Quant. Spectrosc. Radiat. Transfer*, **79–80**, 1159–1169.